https://doi.org/10.1016/j.jes.2022.12.027



# Characterization of a Smog Chamber for Studying Formation of Gas-phase Products and Secondary Organic Aerosol

Qi Yuan[1], Zhuozhi Zhang[1], Meng Wang[1], Kin Fai Ho[2], Tao Wang[1], Shuncheng Lee[1*]

[1] *Department of Civil and Environmental Engineering, The Hong Kong Polytechnic University*

[2] *School of Public Health and Primary Care, The Chinese University of Hong Kong, Shatin, Hong Kong, China*

[*]To Whom Correspondence Should be addressed

E-mail: shun-cheng.lee@polyu.edu.hk

Tel: +852 27666011

**Highlights**

A smog chamber was designed and comprehensively characterized.

The wall loss of gases and particles are smaller than other chambers.

The chamber can provide high quality data for gas-phase oxidation and SOA formation.

Graphical Abstract

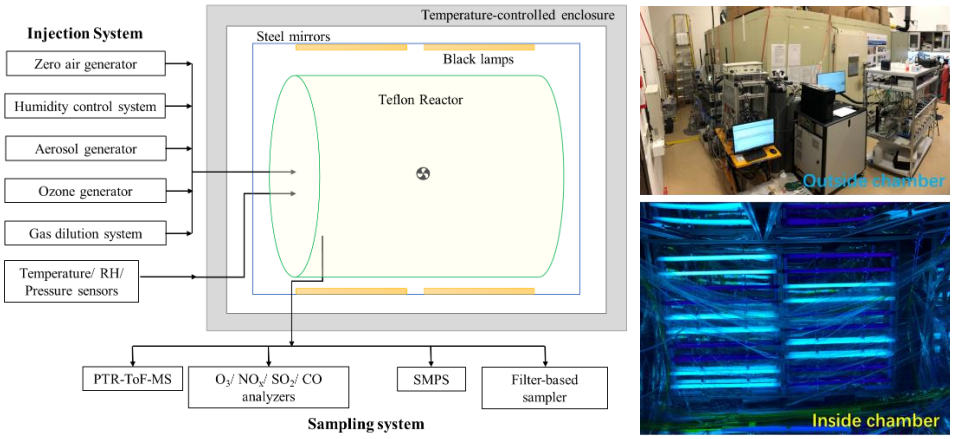

## Conflict of Interest

The authors confirm that there is no conflict of interest to be declared.

# Characterization of a Smog Chamber for Studying Formation of Gas-phase Products and Secondary Organic Aerosol

Qi Yuan[1], Zhuozhi Zhang[1], Meng Wang[1], Kin Fai Ho[2], Tao Wang[1], Shuncheng Lee[1,*]

1. Department of Civil and Environmental Engineering, The Hong Kong Polytechnic University
2. School of Public Health and Primary Care, The Chinese University of Hong Kong, Shatin, Hong Kong, China

**Abstract**: Smog chambers provide a potent approach to explore the secondary organic aerosol formation under varied conditions. This study describes the construction and characterization of a new smog chamber facility for studying the formation mechanisms of gas-phase products and secondary organic aerosol from the photooxidation of volatile organic compounds. The chamber is a 5.4 $m^3$ Fluorinated Ethylene Propylene (FEP) Teflon reactor with the potential to perform photooxidation experiments at controlled temperature and relative humidity. Detailed characterizations were conducted for evaluation of stability of environmental parameters, mixing time, background contamination, light intensity, and wall losses of gases and particles. The photolysis rate of $NO_2$ ($J_{NO2}$) ranged from (1.02−3.32) $\times 10^{-3}$ $sec^{-1}$, comparable to the average $J_{NO2}$ in ambient environment. The wall loss rates for NO, $NO_2$, and $O_3$ were $0.47\times10^{-4}$, $0.37\times10^{-4}$, and $1.17\times10^{-4}$ $min^{-1}$, while wall loss of toluene was obsoletely found in a 6-hours test. The particle number wall loss rates are (0.01−2.46) $\times 10^{-3}$ $min^{-1}$ for 40−350 nm with an average lifetime of more than one day. A series of toluene photooxidation experiments were carried out in absence of $NO_x$ under dry conditions. The results of the simulation experiments demonstrated that the chamber is well designed to simulate photolysis progress in the atmosphere.

**Keywords:**
Smog chamber
Gas-phase oxidation
Chamber characterization
Chemical mechanism

---

*Corresponding author. E-mail: shun-cheng.lee@polyu.edu.hk (S.C. Lee)

## Introduction

Atmospheric chemical processes of volatile organic compounds (VOCs) lead to a variety of secondary oxidized products in the gas phase and particle phase. Such pollutants are often harmful to human health and play important roles in climate change and global atmospheric chemistry (Hallquist et al., 2009; Harrison and Yin, 2000). In real atmosphere, the chemical processes are not easily studied since atmospheric pollutants would undergo not only chemical production and loss, but also emission, transportation, and deposition (Brasseur, 2017). To isolate the chemical processes from other atmospheric processes, smog chambers have been developed to better investigate the near-ground ozone ($O_3$) formation, mechanisms of secondary organic aerosol (SOA) formation, kinetics and mechanisms of multiphase reactions, and ageing processes of primarily emitted pollutants (Babar et al., 2017; Carter et al., 2005; Cocker et al., 2001; Karl et al., 2004; Paulsen et al., 2005; Saathoff et al., 2003; Wang et al., 2011).

With the aid of smog chamber experiments, the VOC oxidation mechanisms, the key factors affecting oxidation, and the SOA yield were revealed. In earlier stages, the chambers were aimed to simulate atmospheric processes under near-real atmospheric conditions to promote the development of air quality models. Based on the results from chamber studies on the oxidation of large quantalities of VOCs, several atmospheric chemical mechanisms were developed, including Statewide Air Pollution Research

Center Mechanism (SAPRC), Regional Atmospheric Chemical Mechanism (RACM), and Master Chemical Mechanism (MCM) (Chu et al., 2021). Among those mechanisms, reactions of hydroperoxyl radical (OH) with VOCs were dominant removal processes, determining the atmospheric lifetime of VOCs. The formation of alkyl radicals, alkoxyl radicals, alkyl peroxy radicals ($RO_2$) and Criegee intermediates were considered as the main transformation pathways of VOCs in the atmosphere (Hallquist et al., 2009). With the innovation of detection techniques, more generations of oxidation products with different volatility were identified in molecular levels, which facilitates the identification of new mechanisms and formation pathways (e.g., new particle formation and autooxidation) (Guo et al., 2020; Pye et al., 2019). Despite the extensive chamber studies on oxidation of VOCs, there are great divergences in the reaction pathways and SOA yields. Taking aromatic hydrocarbons as an example, many new oxidation mechanisms were proposed, e.g., formation of polyhydroxyl compounds from phenolic compounds, autoxidation of highly oxygenated compounds, and hydrogen transfer of aldehydes (Li et al., 2021b; Srivastava et al., 2022). These uncertainties of mechanisms causes the yield of intermediates (e.g., phenol, glyoxal, and methylglyoxal) differs up to 10 times in different studies, which leads to 25%~50% loss of organic carbon in aromatic SOA (Song, 2021). Furthermore, the oxidation durations in past chamber studies are less than the equivalent of 1 day at typical atmospheric oxidation concentrations, which may not fully characterize the production and ageing of secondary organic compounds associated with multiple generations of oxidation (Garmash et al., 2020). Thus, a better understanding of gaseous oxidation of VOCs and SOA chemical properties is required to improve simulation of missing SOA in atmospheric models through laboratory studies.

The construction of smog chambers varied widely in terms of the operating environments, chamber sizes, light sources, and reactor materials to reach different research purposes. Regarding the light sources used and chamber size needed, the smog chambers were usually constructed in indoor and outdoor environment. Taking

advantage of the natural solar radiation and with no size limitation from indoor environment, outdoor chambers can be as large as 270 $m^3$ (Rohrer et al., 2005), while indoor chambers are built with a size range of 1–90 $m^3$ (Wagner et al., 2011; Wu et al., 2007). Comparing with that of outdoor chambers, the operating conditions e.g. (temperature, relative humidity (RH), pressure and light intensity) of indoor chambers can be rapidly, precisely, and stably controlled. This would lead to more atmospheric relevant conditions for simulation experiments and less uncertainty of experiment results (Li et al., 2021a; Wagner et al., 2011). Meanwhile, the larger surface to volume ratios of small chambers enhance the wall effects to some extent. Light sources used in indoor chambers are normally solar, arc and black lights (White et al., 2018). Solar and arc lights are preferred due to their similarity to sunlight, while blacklights are often used for their price advantage. Recent-built chambers combine different types of black lamps with varied wavelength range (280−400 nm) as light sources (Chu et al., 2021). Although these ultraviolet (UV) lights have different spectra with solar radiation, their photolysis rates can be characterized to well simulate the relevant atmospheric conditions. It is worth noting that in some cases the reaction rates would be affected by light sources with different wavelength ranges with solar light (Carter et al., 2005). Common chamber walls or reactors are made of stainless steel, aluminum, Pyrex, quartz, PFA (perfluoroalkoxy alkanes) Teflon, and FEP (fluorinated ethylene propylene) Teflon. Due to the good chemical resistance, high light transmission rate, and adjustability of volume, FEP Teflon film is most used both as reactor material and as coating material inside metallic reactors (Bloss et al., 2005a; Chu et al., 2021; Shao et al., 2022; Wang et al., 2014).

In this study, a new indoor photochemical chamber was built in the air laboratory at the Hong Kong Polytechnic University (PolyU chamber) to study the formation mechanisms of gas-phase products and SOA from photooxidation of aromatic VOCs. Characterization experiments on stability of environmental conditions, mixing time, purity of zero air, photolysis rates of nitrogen dioxide ($NO_2$), and wall loss of gases and

particles were conducted. In addition, photooxidation experiments on a typical aromatic hydrocarbon, toluene, in the absence of nitrogen oxides ($NO_x$) were conducted to examine the performance of the chamber.

## 1 Description of the PolyU chamber

The PolyU chamber is operated in batch mode, in which the composition of the gaseous precursors, aerosol seed, UV lights, temperature, and RH are controlled throughout the duration of several hours. It is composed of three parts: the inner Teflon reactor with frame, the in-between light sources on stainless steel mirrors, and the outer temperature-controlled enclosure. It is equipped with a set of air purification system, gas/aerosol generators, analytical instruments for gases and VOCs, and particle analysis instruments. The schematic of the chamber along with the instruments is shown in Fig. 1.

### 1.1 Enclosure and environmental condition control

There are two nested enclosures outside the Teflon reactor. A 3.2 m × 3.2 m × 2.5 m rectangular enclosure comprises a stainless-steel framework with air conditioning ducts is the outermost shell of the chamber. Between the reactor and the walls of the chamber, six polished stainless-steel mirrors surrounding the reactor enable a maximum and homogeneous light intensity. The air conditioning system on the enclosure controls the temperature in a range of 10–40℃, with an accuracy of ±1℃ (Tan et al., 2021). A humidity control system with zero air generator and purified water in a water tank is connected into the reactor with Teflon tubing, providing a wide humidity range of 5%–80%. Three sensors from Beijing Convenient Environmental Tech Co. Ltd are inserted into the Teflon reactor to monitor the temperature, RH, and air pressure.

## 1.2 Teflon reactor

The reactor in this study was made of 75 μm FEP Teflon material which is chemically inert, resistant to most chemicals, and with high transmittance (> 95%) of UV light. It has a volume of 5.4 $m^3$ (Ø 1.7 m × 2.4 m) and a surface to volume ratio of 1.59 $m^{-1}$. Compared with stainless steel and quartz, the weakness of FEP film is the accumulation of electrostatic charge which can increase the wall loss rates for particles with a diameter smaller than 500 nm (McMurry and Grosjean, 1985). To reduce the effect of electrostatic charge on particle wall loss, two ionizing air blowers are installed outside the reactor at diagonal positions to keep the air flow evenly across the surface of the reactor. The effects of ionizing air blowers were discussed in Section 3.4. The reactor is compression-sealed and suspended in the enclosure and mounted within the rectangle frame. It is flexible to be moved horizontally to maintain a differential positive pressure, minimizing contamination and dilution from air outside. A pressure sensor is used to measure the pressure inside the reactor with an accuracy of ± 3 Pa. The experiments lasted for 4 to 6 hours before the reactor volume decreases to 2/5 of its maximum value. There are seven Teflon ports for injection of purified air, VOCs, oxidants ($H_2O_2$ and $O_3$), other gases (e.g., $NO_x$), sampling of gases for online instruments, and vacuuming the chamber for cleaning. Two additional stainless-steel ports connected with conductive silicone tube are for injection and sampling of particles. One stainless steel fan coated with Teflon is installed at the bottom to accelerate the mixing of reactants. No detectable VOCs are emitted from the fans.

## 1.3 Light sources

To simulate photochemical processes, a total of 42 UV lights are arranged on two opposite sides of the stainless-steel mirrors as the light source to approximate the atmospheric actinic spectrum. Forty of the black lights (36 W, Philips and 36 W, Huaqiang) provide UV-A type light with wavelength ranges of 320−400 nm (center at 340 nm) and 340−400 nm (center at 350 nm). Two UV-C type lamps (40 W, Philips)

provide lights with a center wavelength of 254 nm. The forty UV-A lamps are controlled in 20 groups, and the two UV-C lamps can be controlled independently. Therefore, the light intensity can be regulated into several levels. Due to the space limit of the outer enclosure, the distance between the lights and the reactor is ~ 50 cm. The unwanted heat generated from the irradiation source is removed by the air conditioning system on the enclosure.

### 1.4 Chamber air purification, conditioning, and injection system

A zero-air generator (T701H, Teledyne API) provides clean and dry air at a flow of 20 L/min by passing compressed ambient air at ~ 30 psi. The zero-air generator contains a dryer, an activated charcoal filter, and a chemical scrubber to provide air with free of $NO_x$, $O_3$, CO, $SO_2$, VOCs and particles. The clean air can be conditioned by passing through the humidifier, ozone generator, VOC liquid injection unit and aerosol mixing tank before entering the chamber.

Gaseous reactants (e.g., $NO_x$ and VOCs) are injected from commercially prepared gas cylinders with target gases in nitrogen via a FEP Teflon line into the reactor, and then flushed by purified dry air or nitrogen. For the injection of liquid reactants, certain amount of the liquids with known concentrations are introduced into a U-type three-way injection tube with microliter syringes, and then the liquids are heated and blew into the chamber by pure nitrogen. Ozone is generated by a commercial ozone generator (Model 2001; Jelight Company, USA) with purified air from the zero-air generator. Seed particles are generated by an atomizer (Model 3079; TSI Incorporated, USA) with $(NH_4)_2SO_4$ solution through conductive silicon tubing into the reactor. The flow rate and gas volume of injection are controlled with mass flow controllers.

### 1.5 Instrumentation

The chamber is equipped with advanced instrumentations to measure the gaseous and particulate chemical composition, including trace gases ($O_3$, $NO_x$ and $NO_y$), VOCs,

oxygenated VOCs (OVOCs), particle number and size distribution, and particulate oxygenated products. The species/ parameters to be measured and details on the instrumentation are summarized in **Table 1**. Briefly, $NO_x$ and $O_3$ are measured by Teledyne T series with the accuracy of 0.5%. A large variety of VOCs and OVOCs are quantified in real-time by a PTR-TOF-MS (QiTOF, IONICON, Austria) with a high sensitivity (< 10 pptv) and fast response time (1 sec). With the selective reagent ionization function, reagent ions in PTR-TOF-MS can be switched among $H_3O^+$, $O_2^+$ and $NO^+$, thus enhancing the analyzable compound classes and increasing selectivity. OVOCs with more functional groups can be measured by a high-resolution time-of flight chemical ionization mass spectrometer (HR-ToF-CIMS, Aerodyne) with nitrate or iodide as reagent ions. In addition to the OVOCs, oxygenated products in SOA are measured with online and offline approaches. A filter-inlet for gases and aerosols (FIGAERO) is optionally coupled to the HR-ToF-CIMS to measure the semi- and low-volatile organic compounds in particulate matters. Offline samples are collected with a custom-built sampler with 47 mm filters at 20 L/min, and then analyzed with an Orbitrap Fusion Lumos mass spectrometer coupled with a liquid chromatography (LC-Orbitrap MS, Thermo Scientific). Aerosol size and number distribution are monitored by a scanning mobility particle sizer (SMPS) which consists of a differential mobility analyzer (3082 DMA, TSI, USA) and a condensation particle counter (3776 CPC, TSI, USA). Environmental parameters, i.e., temperature,RH, and pressure, are monitored with sensors from Beijing Convenient Environmental Tech Co.Ltd.

## 2 Characterization of the chamber

### 2.1 Stability of RH, temperature, and control of mixing

Temperature and humidity are two important environmental parameters during chemical processes. The temperature inside the reactor is controlled by the air conditioning system of the chamber enclosure by presetting a targeted value to keep a stable experimental condition and avoid overheating by UV lights. Water vapor is

flushed into the chamber by bubbling deionized water with a certain flow of purified air until RH reaches set point. A temperature of 25℃ and a RH of 50% were set to examine the stability of the system with and without UV light irradiation. **Fig. 2(a)** shows the evolution of temperature and RH during the test. The temperature and humidity reached the set point during the first 20 minutes and then remained stable under dark conditions. Once all the 42 lights were turned on, temperature increased from 25℃ to ~27℃ in 10 minutes and then stayed at 26.0 ± 0.4℃. The increase of temperature caused the slight drop (1%) of RH. The results showed that although there is unwanted heating when lights are turned on, temperature and RH can be well controlled for stable and repeatable experiments.

Mixing time of gases were tested with $NO_2$ and toluene as tracers. Before the injection of gases, the mixing fan was turned on with full speed. Considering the volume of the chamber and the mixing ratios of gases, 177 ppm $NO_2$ and 32 ppm toluene were injected into the chamber at 1.22 L/min and 5.6 L/min for 3 minutes to reach ~120 ppb and ~100 ppb, respectively. **Fig. 2(b)** shows that the mixing of gases is within 5 minutes from the beginning of the injection, comparable to that of few minutes in other smog chambers (Shao et al., 2022; Wang et al., 2014).

### 2.2 Background contamination of the chamber

After cleaning procedure of the chamber, the background level of contaminants in the chamber should be examined and kept as low as possible, especially for the tests carried out with atmospherically relevant concentrations. Hydrocarbons and OVOCs in the chamber were below detection limit of PTR-TOF-MS. Results of air purity test in chamber are shown in **Fig. 3**. $NO_x$ and $O_3$ are detected to be lower than 1 ppb after cleaning. And particle number concentration inside the chamber is less than 10 $cm^{-3}$ in number and ~ 0 $\mu g/m^3$. After seven hours photooxidation of zero air, minimal particle formation of number concentration at < $10^3$ $cm^{-3}$ and mass concentration < 0.6 $\mu g/m^3$ was observed, respectively. Approximately 4 ppb of $O_3$ was generated after seven hours

irradiation, with a formation rate of 0.63 ppb/hr. The formation rates of SOA and $O_3$ were comparable to previous studies on characterization of chambers (Babar et al., 2017; Hu et al., 2014; Ma et al., 2022; Wu et al., 2007). The formation of particle concentration and $O_3$ from photolysis of zero air is minimal compared with SOA formed in normal experimental conditions (> 20 μg/m$^3$), proving that pollutants levels in zero air would cause negligible effects on experimental results in our study.

**2.3 Light intensity**

The artificial radiation has a broad radiation distribution owing to the chosen combination of illumination sources, producing irradiation over the wavelength range 200-400 nm. Light intensity is represented by the photolysis rate of $NO_2$, which is estimated through injecting $NO_2$ standard gas into the reactor, then irradiating the $NO_2$ in chamber with varied light intensities, and measuring the concentrations of NO, $NO_2$ and $O_3$. The photolysis rate of $NO_2$ ($J_{NO2}$) is estimated with the following equation

$$J_{NO_2} = k_{NO+O_3}[NO][O_3]/[NO_2] \quad (1)$$

where *[NO]*, *[$O_3$]* and *[$NO_2$]* represent concentrations (molecule/cm$^3$) of the gases, and $k_{NO+O3}$ = 1.95 × 10$^{-14}$ cm$^3$/(mol·sec) (Atkinson et al., 2004) is the rate constant of $O_3$ and NO reaction. A series of $NO_2$ actinometry experiments were carried out with different number of UV lights turned on. With the setting ranging from 25% (6 of 340 nm and 4 of 350 nm wavelength lamps) to 100% (all lamps) of the lights turned on, the J values ranged from 1.02 × 10$^{-3}$ sec$^{-1}$ to 3.32 × 10$^{-3}$ sec$^{-1}$ (**Fig. 4**). The maximum $NO_2$ photolysis rate (3.32 × 10$^{-3}$ sec$^{-1}$) in our chamber is comparable to those reported in other chambers provided in **Table 2**, e.g., (2.32−2.55) × 10$^{-3}$ sec$^{-1}$ in the 5 m$^3$ chamber at the Institute of Chemistry, Chinese Academy of Sciences dual reactor chamber (ICCAS-DRC) (Wang et al., 2015), and 2.83 × 10$^{-3}$ sec$^{-1}$ in the 7 m$^3$ chamber at the Kyungpook National University (Babar et al., 2017). The maximum $J_{NO2}$ value of our chamber is comparable to the average ambient values during the late summer and autumn, i.e., (2.28 ± 2.80) × 10$^{-3}$ sec$^{-1}$ and (2.12 ± 2.78) × 10$^{-3}$ sec$^{-1}$, and the lower $J_{NO2}$

values with half lights turned on is comparable to the ambient values in winter ((1.56 ± 2.35) × $10^{-3}$ $sec^{-1}$) in Hong Kong (Li et al., 2018), which shows that the light system is capable of simulating the ambient photochemistry in different seasons.

The heat generated by the UV lights in indoor chambers and trapped in Teflon reactors may affect the reaction rates of VOCs and the gases. With all the lamps on, we carefully monitored the variation of temperature and used the control system to slightly adjust it. The typical change of temperature in the reactor is less than 2℃ after 6 hours of use.

**2.4 Wall loss of gases and particles**

Adsorption of gases had been shown to be a substantial source of gas losses inside Teflon bags which influences the gas-phase reactivity and SOA formation (Grosjean, 1985). In the PolyU chamber, the wall loss rates of NO, $NO_2$, $O_3$ and toluene were investigated by injecting known concentrations of gases into the chamber and measuring their concentration decay for an extended period under dark conditions (**Fig. 5**). Approximately 450 ppb NO, 120 ppb $NO_2$ and 500 ppb $O_3$, and 100 ppb toluene were separately injected into the chamber and monitored for 6 hours allowing sufficient time for a measurable decay. All the wall loss experiments of gaseous species were conducted under the temperature and RH of ~25°C and < 10% respectively. The wall loss rates of NO, $NO_2$, $O_3$ in our chamber are 0.47 × $10^{-4}$, 0.37 × $10^{-4}$, and 1.17 × $10^{-4}$ $min^{-1}$, respectively. The concentration of toluene remained 96.491 ± 0.291 ppb during the wall loss test. It suggested that negligible wall loss for toluene was observed in PolyU chamber, which is similar to that reported by Wang et al. (2011), Hu et al. (2014), and Babar et al. (2017). The wall loss rates of these gases in our chamber are 2–10 times lower than those of other chambers (**Table 2**).

Particle deposition onto the surface of the reactor is recognized to be influenced by diffusion, coagulation of the particles as a function of particle size, and the charged wall

materials (Grosjean, 1985). The particle number wall loss rate is described by first-order kinetics as

$$dN(d_p,t)/dt = -K_N(d_p)N(d_p,t) \quad (2)$$

where $N(d_p,t)$ is the particle number concentration, $d_p$ is the diameter of the particle and $K_N(d_p)$ is the particle number loss coefficient (Cocker et al., 2001). The $K_N(d_p)$ values can be estimated from the decrease of particle number concentration versus time when no new particles are formed or injected into the chamber. In this study, 0.5 mol/L ammonium sulfate ($(NH_4)_2SO_4$, AS) solution was atomized to generate seed particles. The AS particles were introduced into the reactor with a flow rate of 1.5 L/min for 10 minutes and diluted to ~8000 $cm^{-3}$ to reduce the coagulation of smaller particles. The changing of particle distribution is shown in **Fig. 6**. In general, the particle wall loss rates of the PolyU chamber were (0.01−2.46) × $10^{-3}$ $min^{-1}$ within 40–350 nm, corresponding to an average lifetime of ~25 hr. For particle diameters of 100 nm, the wall loss rate is 0.2 × $10^{-3}$ $min^{-1}$ (**Table 2**), comparable to that of the CESAM chamber in France (Wang et al., 2011), but smaller than the value of (1.33−4.3) × $10^{-3}$ $min^{-1}$ reported in other chambers with similar volumes (Babar et al., 2017; Bae et al., 2003; Ma et al., 2022; Smith et al., 2019; Wang et al., 2015; Wu et al., 2007). The lower wall losses of gases and particles in this study is probably due to smaller surface-to-volume area (1.59 $m^{-1}$) and the removal of static electricity from ionizing air blowers.

### 2.5 Experiment of toluene photooxidation

A sequence of experiments on OVOC and SOA formation from toluene photooxidation has been performed to validate the utility of PolyU chamber for studying SOA formation and atmospheric chemistry. This reaction system has been widely studied for the yields of gas-phase products and SOA, and the impact of some factors SOA formation (Chen et al., 2019; Hildebrandt Ruiz et al., 2015; Hinks et al., 2018; Ng et al., 2007; Qi et al., 2020; Sato et al., 2007). The initial conditions and yield for each experiment are presented in **Table 3**. All the experiments were conducted without

aerosol seed at a temperature of 25 ± 0.5℃ and dry conditions (RH＜10%). In general, 200 μL of $H_2O_2$ solution was injected into a U-type glass tube and blew into the chamber by pure nitrogen, afterwards 73–155 ppb of toluene was injected into the chamber. After turning the UV lights on, $H_2O_2$ was rapidly converted into OH radical, leading to the decay of toluene and formation of OVOCs and SOA. Mass concentrations of SOA were calculated from the corrected volume concentrations by setting the particle density as 1.4 g/cm$^3$ based on literature data (Nakao et al., 2011; Ng et al., 2007; Sato et al., 2007).

The concentrations of toluene and gas-phase oxidation products were tracked with PTR-TOF-MS. **Fig. 7** shows a comparison of mass spectra from one typical test before UV lights on and after at least 5 hours of irradiation. The mass peaks at m/z 31.017, 47.012, 61.028, 73.028, 77.022, 85.028, 99.007, 107.049, 109.065, and 123.044 were assigned to $CH_2O$ (formaldehyde), $CH_2O_2$ (formic acid), $C_2H_4O_2$ (acetic acid), $C_3H_4O_2$ (methylglyoxal), $C_2H_4O_3$ (peracetic acid), $C_4H_4O_2$ (butenedial/furanone), $C_4H_2O_3$ (maleic anhydride), $C_7H_6O$ (benzaldehyde), $C_7H_8O$ (cresol), and $C_7H_6O_2$ (p-methyl benzoquinone). The simplified formation pathways of the products from toluene photooxidation implemented in Master Chemical Mechanism (MCM) v3.3.1 are listed in **Fig. 8**. Benzaldehyde was formed as a first-generation product from OH-initiated H-abstraction from the methyl group of toluene, while the formation of products from phenol, peroxide-bicyclic ring-opening, and the epoxy-oxy channels are initiated by OH adduction on the aromatic ring. Cresols are formed by elimination of hydroperoxyl radical from phenol route, and the OH addition of it further produces *p*-methyl-benzoquinone as a second-generation product. Peroxide-bicyclic routes generates methyl substituted peroxide radicals, resulting in the direct formation of ring-opening products, i.e., butenedial, furanone, and methylglyoxal, following the formation of maleic anhydride as the second-generation products. Intermediate of epoxy route, 2,3-Epoxy-6-oxo-4-heptenal (not detected), further reacts and for methylglyoxal and formaldehyde as the second-generation products. Multi-generation oxidation of the first- and second-generation of products sequentially forms small molecule carbonyls,

362 i.e., formaldehyde, formic acid, acetic acid, methylglyoxal, and peracetic acid.

363 The proposed yields of products from the four routes as implemented in MCM are
364 higher than that in this study. For instance, the yields of benzaldehyde and cresol are
365 0.5%−2% and 1%−6% in this study versus 7% and 18% in MCM, respectively. It should
366 be noted that MCM provides yields of stable, volatile early-generation products, which
367 means the yields of these OVOCs would be different in ageing processes (Bloss et al.,
368 2005b). To be specific, reactions of reactive OVOCs can be further oxidized into other
369 products, leading to lower gas-phase product yield. High yields of later generation
370 products, formic acid (17%−27%), acetic acid (12%−17%) and peracetic acid (2%−5%)
371 were observed in this study (**Fig. 9**). It agrees well with the fact that excess $H_2O_2$
372 injection results in the ageing processes in our tests and prompted the production of
373 multi-generation products. On the other hand, yield of intermediate products varied
374 under different $NO_x$ conditions (Arey et al., 2009; Chen et al., 2019; Gómez Alvarez et
375 al., 2007). In this study, we performed the toluene photooxidation experiments in
376 absence of $NO_x$. It's shown by Song et al. (2021) that yield of methylglyoxal and
377 benzaldehyde could be 10−20 times lower under no $NO_x$ conditions than that under
378 high $NO_x$ conditions, which is in good agreement with the current study. Furthermore,
379 a near-explicit mechanism of toluene from MCM version 3.3.1 using the Frame-work
380 for 0-D Atmospheric Modeling (F0AM) was applied to simulate the toluene
381 photooxidation. The description of F0AM in detail can be seen in the supporting
382 information. The time series of the selected compounds from model and experimental
383 results were compared in **Appendix A Fig. S1** and **Fig. S2**. Toluene was consumed faster
384 in experimental measurements than in model results. As first-generation products,
385 benzaldehyde and cresols are predicted to be 4 times higher than in experimental results,
386 whilst the further generation products are much higher in experimental results than that in
387 model results. These trends indicate that the oxidation was accelerated and aged in our
388 experiment. It should be noted that the $J_{NO2}$ input in F0AM was acquired from experiments
389 on photolysis rate of $NO_2$ in chamber. Different from other reactions, $NO_2$ cannot be

photolyzed by UV light under 300 nm. The two 254 nm wavelength UV lights would be an important cause of the discrepancy between model and experimental results.

As shown in **Fig. 9**, slope of the growth curve of OVOC yields as a function of OVOC mass concentration ($M_0$) showed dependence on initial toluene concentration. With higher initial toluene concentration, the first-generation products (benzaldehyde and cresols) showed higher yields with a much faster rate of growth. After some irradiated time, the yield of benzaldehyde and cresols decreased with the increment of $M_0$, which refers to the consumption of these OVOCs and potential production of further generation products and SOA (Chen et al., 2019). As later-generation products, acids (formic, acetic and peracetic acids) grow with higher slopes when initial concentration of toluene is lower. Meanwhile, the peak of SOA number concentration appeared earlier and stronger along with lower initial concentration of toluene (**Fig. 10**). These phenomena are in line with the findings that the first-generation products compete with toluene on consumption of OH radical, leading to a faster formation of intermediate VOCs, and promoting the formation of further generation products in gas- and particle-phase(Atkinson and Arey, 2003; Chen et al., 2019; Ng et al., 2007).

In the photooxidation of toluene under dry conditions with no seed and $NO_x$, the SOA yield varied from 24.7%−34.3%, comparable to those of Hinks et al. (2018), Hildebrandt Ruiz et al. (2015), and Ng et al. (2007) (**Table 4**). The high SOA yield under no $NO_x$ conditions is likely due to no competition between $NO_x$ and $HO_2$ to reaction with $RO_2$, which is indicated by other studies under low $NO_x$ conditions with much lower yield with a range of 1.9%−17% (Chen et al., 2019; Qi et al., 2020; Sato et al., 2007). To be noted, the excess OH would cause ageing of SOA, leading to a higher SOA yield (Hildebrandt Ruiz et al., 2015). With higher precursor concentrations, intermediates are quickly oxidized into SOA, following the size increasing in ageing processes (**Fig. 10**).

## 3 Conclusions

We built an indoor smog chamber system to study VOC photooxidation and SOA formation progress close to the real atmospheric environment. State-of-the-art on-line instruments for monitoring gas-phase and particle-phase oxidation products have been equipped in our system. A series of characterization experiments have been conducted, showing that our system is with good temperature and humidity stability, high mixing efficiency, low contamination of background air, small wall loss of gases and particles, and moderate light intensity compared with other chambers and ambient environment. The yields of photooxidation of toluene under dry conditions in absence of $NO_x$ showed good agreement with previous studies under similar experimental conditions. OVOCs and SOA formation depends on the initial concentrations of toluene and OH radical. With higher concentrations of toluene, faster consumption of intermediates and formation of later generation products and SOA were observed. The overdose $H_2O_2$ results in excess OH, which aggravated the ageing processes of toluene oxidation products. These results illustrate that our chamber can be used for investigation of transformation of gas-phase pollutants and SOA formation and ageing processes.

## Authorship Contribution Statement

**Qi Yuan:** Data curation, Formal analysis, Investigation, Methodology, Writing-original draft, Writing-review & editing

**Zhuozhi Zhang:** Formal analysis, Software, Writing-review & editing

**Meng Wang:** Methodology, Writing-review & editing

**Kin Fai Ho:** Funding acquisition, Methodology, Supervision

**Tao Wang:** Funding acquisition, Methodology

**Shun-cheng Lee:** Funding acquisition, Methodology, Supervision, Writing-review & editing


## Acknowledgement

This research was financially supported by the Research Grants Council (RGC) of Hong Kong Special Administrative Region, China (T24-504/17-N). The authors would like to acknowledge the HKPolyU University Research Facility in Chemical and Environmental Analysis (UCEA) for the equipment support. The authors are grateful to Dr. Yi Chen from Hong Kong University of Science and Technology for the inspiration and discussion on the characterization experiments.

## Reference


Arey, J., Obermeyer, G., Aschmann, S.M., Chattopadhyay, S., Cusick, R.D., and Atkinson, R., 2009. Dicarbonyl products of the OH radical-initiated reaction of a series of aromatic hydrocarbons, Environ. Sci. Technol., 43, 683-689.

Atkinson, R., and Arey, J., 2003. Atmospheric Degradation of Volatile Organic Compounds, Chem. Rev., 103, 4605-4638.

Atkinson, R., Baulch, D.L., Cox, R.A., Crowley, J.N., Hampson, R.F., Hynes, R.G., Jenkin, M.E., Rossi, M.J., and Troe, J., 2004. Evaluated kinetic and photochemical data for atmospheric chemistry: Volume I - gas phase reactions of $O_x$, $HO_x$, $NO_x$ and $SO_x$ species, Atmos. Chem. Phys., 4, 1461-1738.

Babar, Z.B., Park, J.-H., Kang, J., and Lim, H.-J., 2017. Characterization of a Smog Chamber for Studying Formation and Physicochemical Properties of Secondary Organic Aerosol, Aerosol Air Qual. Res., 16, 3102-3113.

Bae, G., Kim, M., Lee, S., Song, K., Jin, H., and Moon, K., 2003. Design and performance evaluation of the KIST indoor smog chamber, J. Korean Soc. Atmos. Environ., 19, 437-449.

Bloss, C., Wagner, V., Bonzanini, A., Jenkin, M.E., Wirtz, K., Martin-Reviejo, M., and Pilling, M.J., 2005a. Evaluation of detailed aromatic mechanisms (MCMv3 and MCMv3.1) against environmental chamber data, Atmos. Chem. Phys., 5, 623-639.

Bloss, C., Wagner, V., Jenkin, M.E., Volkamer, R., Bloss, W.J., Lee, J.D., Heard, D.E., Wirtz, K., Martin-Reviejo, M., Rea, G., Wenger, J.C., and Pilling, M.J., 2005b. Development of a detailed chemical mechanism (MCMv3.1) for the atmospheric oxidation of aromatic hydrocarbons, Atmos. Chem. Phys., 5, 641-664.

Brasseur, G., & Jacob, D., 2017. Chemical Processes in the Atmosphere, in: Modeling of Atmospheric Chemistry, Cambridge University Press, Cambridge, 54-83.

Carter, W.P.L., Cocker, D.R., Fitz, D.R., Malkina, I.L., Bumiller, K., Sauer, C.G., Pisano, J.T., Bufalino, C., and Song, C., 2005. A new environmental chamber for evaluation of gas-phase chemical mechanisms and secondary aerosol formation, Atmos. Environ., 39, 7768-7788.

Chen, T., Liu, Y., Chu, B., Liu, C., Liu, J., Ge, Y., Ma, Q., Ma, J., and He, H., 2019. Differences of the oxidation process and secondary organic aerosol formation at low and high precursor concentrations, J. Environ. Sci. (China), 79, 256-263.

Chu, B., Chen, T., Liu, Y., Ma, Q., Mu, Y., Wang, Y., Ma, J., Zhang, P., Liu, J., Liu, C., Gui, H., Hu, R., Hu, B., Wang, X., Wang, Y., Liu, J., Xie, P., Chen, J., Liu, Q., Jiang, J., Li, J., He, K., Liu, W., Jiang, G., Hao, J., and He, H., 2021. Application of smog chambers in atmospheric process studies, Natl. Sci. Rev., 9.

Cocker, D.R., Flagan, R.C., and Seinfeld, J.H., 2001. State-of-the-Art Chamber Facility for Studying Atmospheric Aerosol Chemistry, Environ. Sci. Technol., 35, 2594-2601.

Garmash, O., Rissanen, M.P., Pullinen, I., Schmitt, S., Kausiala, O., Tillmann, R., Zhao, D., Percival, C., Bannan, T.J., Priestley, M., Hallquist, Å.M., Kleist, E., Kiendler-Scharr, A., Hallquist, M., Berndt, T., McFiggans, G., Wildt, J., Mentel, T.F., and Ehn, M., 2020. Multi-generation OH oxidation as a source for highly oxygenated organic molecules from aromatics, Atmos. Chem. Phys., 20, 515-537.

Gómez Alvarez, E., Viidanoja, J., Muñoz, A., Wirtz, K., and Hjorth, J., 2007. Experimental confirmation

494 of the dicarbonyl route in the photo-oxidation of toluene and benzene, Environ. Sci. Technol., 41, 8362-
495 8369.
496 Grosjean, D., 1985. Wall loss of gaseous pollutants in outdoor Teflon chambers, Environ. Sci. Technol.,
497 19, 1059-1065.
498 Guo, S., Hu, M., Peng, J., Wu, Z., Zamora, M.L., Shang, D., Du, Z., Zheng, J., Fang, X., Tang, R., Wu,
499 Y., Zeng, L., Shuai, S., Zhang, W., Wang, Y., Ji, Y., Li, Y., Zhang, A.L., Wang, W., Zhang, F., Zhao, J.,
500 Gong, X., Wang, C., Molina, M.J., and Zhang, R., 2020. Remarkable nucleation and growth of ultrafine
501 particles from vehicular exhaust, 117, 3427-3432.
502 Hallquist, M., Wenger, J.C., Baltensperger, U., Rudich, Y., Simpson, D., Claeys, M., Dommen, J.,
503 Donahue, N.M., George, C., Goldstein, A.H., Hamilton, J.F., Herrmann, H., Hoffmann, T., Iinuma, Y.,
504 Jang, M., Jenkin, M.E., Jimenez, J.L., Kiendler-Scharr, A., Maenhaut, W., McFiggans, G., Mentel, T.F.,
505 Monod, A., Prévôt, A.S.H., Seinfeld, J.H., Surratt, J.D., Szmigielski, R., and Wildt, J., 2009. The
506 formation, properties and impact of secondary organic aerosol: current and emerging issues, Atmos.
507 Chem. Phys., 9, 5155-5236.
508 Harrison, R.M., and Yin, J., 2000. Particulate matter in the atmosphere: which particle properties are
509 important for its effects on health?, Sci. Total. Environ., 249, 85-101.
510 Hildebrandt Ruiz, L., Paciga, A.L., Cerully, K.M., Nenes, A., Donahue, N.M., and Pandis, S.N., 2015.
511 Formation and aging of secondary organic aerosol from toluene: changes in chemical composition,
512 volatility, and hygroscopicity, Atmos. Chem. Phys., 15, 8301-8313.
513 Hinks, M.L., Montoya-Aguilera, J., Ellison, L., Lin, P., Laskin, A., Laskin, J., Shiraiwa, M., Dabdub, D.,
514 and Nizkorodov, S.A., 2018. Effect of relative humidity on the composition of secondary organic aerosol
515 from the oxidation of toluene, Atmos. Chem. Phys., 18, 1643-1652.
516 Hu, C., Cheng, Y., Pan, G., Gai, Y., Gu, X., Zhao, W., Wang, Z., Zhang, W., Chen, J., Liu, F., Shan, X.,
517 and Sheng, L., 2014. A Smog Chamber Facility for Qualitative and Quantitative Study on Atmospheric
518 Chemistry and Secondary Organic Aerosol, Chinese J. Chem. Phys., 27, 631-639.
519 Karl, M., Brauers, T., Dorn, H.-P., Holland, F., Komenda, M., Poppe, D., Rohrer, F., Rupp, L., Schaub,
520 A., and Wahner, A., 2004. Kinetic Study of the OH-isoprene and $O_3$-isoprene reaction in the atmosphere
521 simulation chamber, SAPHIR, Geophys. Res. Lett., 31.
522 Li, J., Li, H., Wang, X., Wang, W., Ge, M., Zhang, H., Zhang, X., Li, K., Chen, Y., Wu, Z., Chai, F.,
523 Meng, F., Mu, Y., Mellouki, A., Bi, F., Zhang, Y., Wu, L., and Liu, Y., 2021a. A large-scale outdoor
524 atmospheric simulation smog chamber for studying atmospheric photochemical processes:
525 Characterization and preliminary application, J. Environ. Sci. (China), 102, 185-197.
526 Li, K., Lin, C., Geng, C., White, S., Chen, L., Bao, Z., Zhang, X., Zhao, Y., Han, L., Yang, W., and Azzi,
527 M., 2020. Characterization of a new smog chamber for evaluating SAPRC gas-phase chemical
528 mechanism, J. Environ. Sci. (China), 95, 14-22.
529 Li, Y., Zhao, J., Wang, Y., Seinfeld, J.H., and Zhang, R., 2021b. Multigeneration Production of Secondary
530 Organic Aerosol from Toluene Photooxidation, Environ. Sci. Technol., 55, 8592-8603.
531 Li, Z., Xue, L., Yang, X., Zha, Q., Tham, Y.J., Yan, C., Louie, P.K.K., Luk, C.W.Y., Wang, T., and Wang,
532 W., 2018. Oxidizing capacity of the rural atmosphere in Hong Kong, Southern China, Sci. Total. Environ.,
533 612, 1114-1122.
534 Ma, W., Liu, Y., Zhang, Y., Feng, Z., Zhan, J., Hua, C., Ma, L., Guo, Y., Zhang, Y., Zhou, W., Yan, C.,
535 Chu, B., Chen, T., Ma, Q., Liu, C., Kulmala, M., Mu, Y., and He, H., 2022. A New Type of Quartz Smog

Chamber: Design and Characterization, Environ. Sci. Technol., 56, 2181-2190.
McMurry, P.H., and Grosjean, D., 1985. Gas and aerosol wall losses in Teflon film smog chambers, Environ. Sci. Technol., 19, 1176-1182.
Nakao, S., Clark, C., Tang, P., Sato, K., and Cocker Iii, D., 2011. Secondary organic aerosol formation from phenolic compounds in the absence of $NO_x$, Atmos. Chem. Phys., 11, 10649-10660.
Ng, N.L., Kroll, J.H., Chan, A.W.H., Chhabra, P.S., Flagan, R.C., and Seinfeld, J.H., 2007. Secondary organic aerosol formation from *m*-xylene, toluene, and benzene, Atmos. Chem. Phys., 7, 3909-3922.
Paulsen, D., Dommen, J., Kalberer, M., Prévôt, A.S.H., Richter, R., Sax, M., Steinbacher, M., Weingartner, E., and Baltensperger, U., 2005. Secondary Organic Aerosol Formation by Irradiation of 1,3,5-Trimethylbenzene−$NO_x$−$H_2O$ in a New Reaction Chamber for Atmospheric Chemistry and Physics, Environ. Sci. Technol., 39, 2668-2678.
Pye, H.O.T., D'Ambro, E.L., Lee, B.H., Schobesberger, S., Takeuchi, M., Zhao, Y., Lopez-Hilfiker, F., Liu, J., Shilling, J.E., Xing, J., Mathur, R., Middlebrook, A.M., Liao, J., Welti, A., Graus, M., Warneke, C., de Gouw, J.A., Holloway, J.S., Ryerson, T.B., Pollack, I.B., and Thornton, J.A., 2019. Anthropogenic enhancements to production of highly oxygenated molecules from autoxidation, Proceedings of the National Academy of Sciences of the United States of America, 116, 6641-6646.
Qi, X., Zhu, S., Zhu, C., Hu, J., Lou, S., Xu, L., Dong, J., and Cheng, P., 2020. Smog chamber study of the effects of $NO_x$ and $NH_3$ on the formation of secondary organic aerosols and optical properties from photo-oxidation of toluene, Sci. Total. Environ., 727, 138632.
Rohrer, F., Bohn, B., Brauers, T., Brüning, D., Johnen, F.J., Wahner, A., and Kleffmann, J., 2005. Characterisation of the photolytic HONO-source in the atmosphere simulation chamber SAPHIR, Atmos. Chem. Phys., 5, 2189-2201.
Saathoff, H., Moehler, O., Schurath, U., Kamm, S., Dippel, B., and Mihelcic, D., 2003. The AIDA soot aerosol characterisation campaign 1999, J. Aerosol Sci., 34, 1277-1296.
Sato, K., Hatakeyama, S., and Imamura, T., 2007. Secondary Organic Aerosol Formation during the Photooxidation of Toluene: NOx Dependence of Chemical Composition, J. Phys. Chem. A, 111, 9796-9808.
Shao, Y., Wang, Y., Du, M., Voliotis, A., Alfarra, M.R., O'Meara, S.P., Turner, S.F., and McFiggans, G., 2022. Characterisation of the Manchester Aerosol Chamber facility, Atmos. Meas. Tech., 15, 539-559.
Smith, D.M., Fiddler, M.N., Sexton, K.G., and Bililign, S., 2019. Construction and Characterization of an Indoor Smog Chamber for Measuring the Optical and Physicochemical Properties of Aging Biomass Burning Aerosols, Aerosol Air Qual. Res., 19, 467-483.
Song, M., Liu, Ying, Li, Xin, Lu, Sihua, 2021. Advances on Atmospheric Oxidation Mechanism of Typical Aromatic Hydrocarbons, Acta Chim. Sin., 79, 1214-1231.
Srivastava, D., Vu, T.V., Tong, S., Shi, Z., and Harrison, R.M., 2022. Formation of secondary organic aerosols from anthropogenic precursors in laboratory studies, npj Climate and Atmospheric Science, 5, 22.
Tan, Y., Liu, C., Ho, K., Ma, Q., and Lee, S.-C., 2021. Characterization of an indoor environmental chamber and identification of C1–C4 OVOCs during isoprene ozonolysis, Indoor. Built Environ., 30, 554-564.
Wagner, R., Möhler, O., Saathoff, H., Schnaiter, M., and Leisner, T., 2011. New cloud chamber experiments on the heterogeneous ice nucleation ability of oxalic acid in the immersion mode, Atmos.

Chem. Phys., 11, 2083-2110.
Wang, J., Doussin, J.F., Perrier, S., Perraudin, E., Katrib, Y., Pangui, E., and Picquet-Varrault, B., 2011. Design of a new multi-phase experimental simulation chamber for atmospheric photosmog, aerosol and cloud chemistry research, Atmos. Meas. Tech., 4, 2465-2494.
Wang, W.-G., Li, K., Zhou, L., Ge, M.-F., Hou, S.-Q., Tong, S.-R., Mu, Y.-J., and Jia, L., 2015. Evaluation and Application of Dual-Reactor Chamber for Studying Atmospheric Oxidation Processes and Mechanisms, Acta Phys. -Chim. Sin., 31, 1251-1259.
Wang, X., Liu, T., Bernard, F., Ding, X., Wen, S., Zhang, Y., Zhang, Z., He, Q., Lü, S., Chen, J., Saunders, S., and Yu, J., 2014. Design and characterization of a smog chamber for studying gas-phase chemical mechanisms and aerosol formation, Atmos. Meas. Tech., 7, 301-313.
White, S., Angove, D., Li, K., Campbell, I., Element, A., Halliburton, B., Lavrencic, S., Cameron, D., Jamie, I., and Azzi, M., 2018. Development of a new smog chamber for studying the impact of different UV lamps on SAPRC chemical mechanism predictions and aerosol formation, Environ. Chem., 15, 171-182.
Wu, S., Lü, Z., Hao, J., Zhao, Z., Li, J., Takekawa, H., Minoura, H., and Yasuda, A., 2007. Construction and characterization of an atmospheric simulation smog chamber, Adv. Atmos. Sci., 24, 250-258.

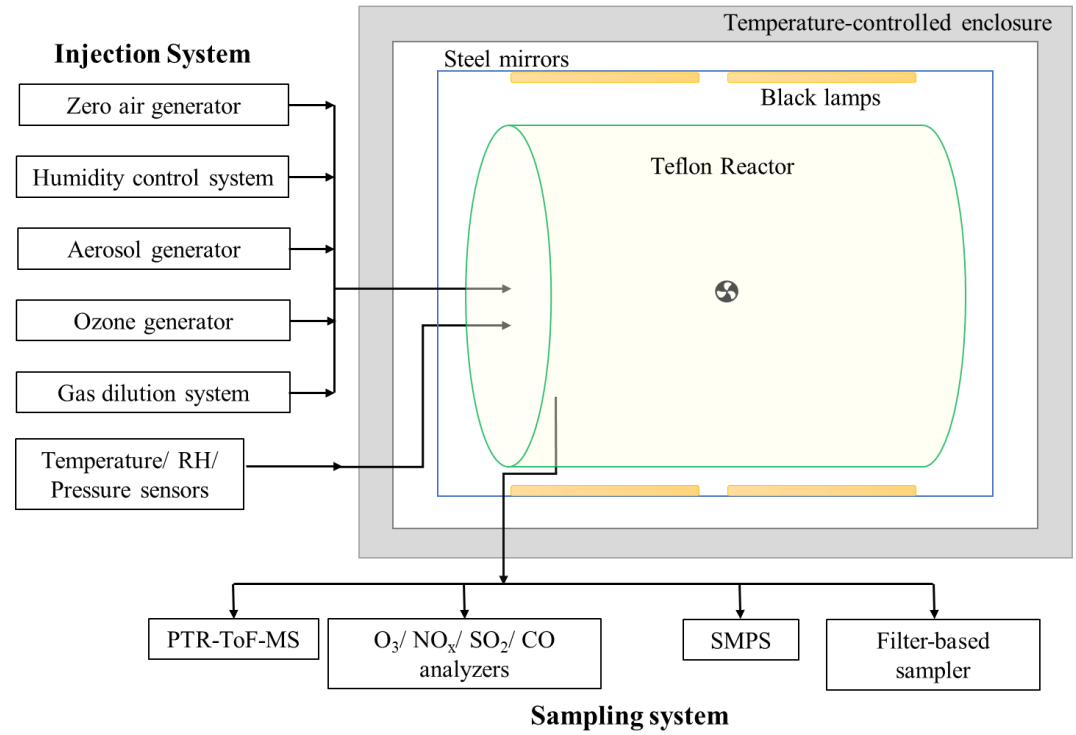


**Figure 1.** The schematics of the PolyU smog chamber facility.

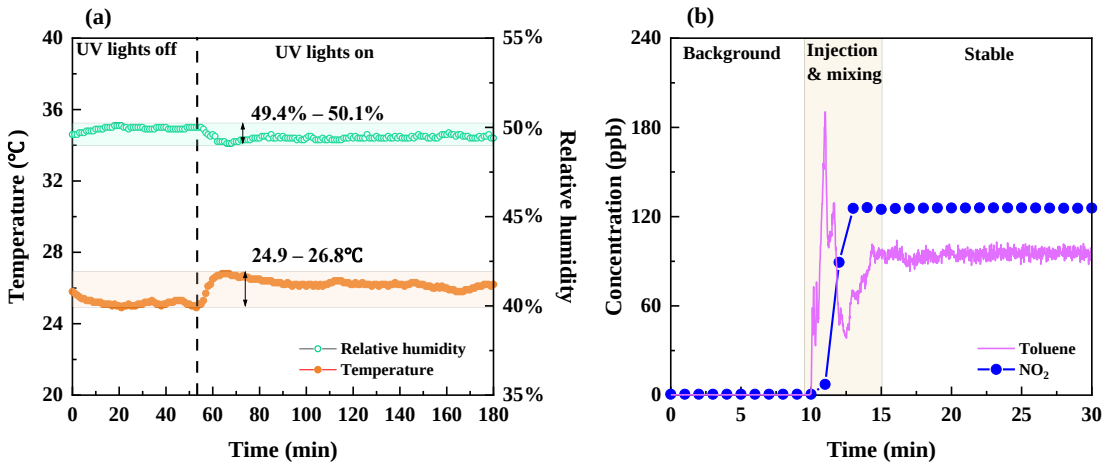


**Figure 2.** Evolution of (a) temperature and relative humidity inside the chamber with lights off and 42 lights on, (b) toluene and $NO_2$ before, during and after the injection.

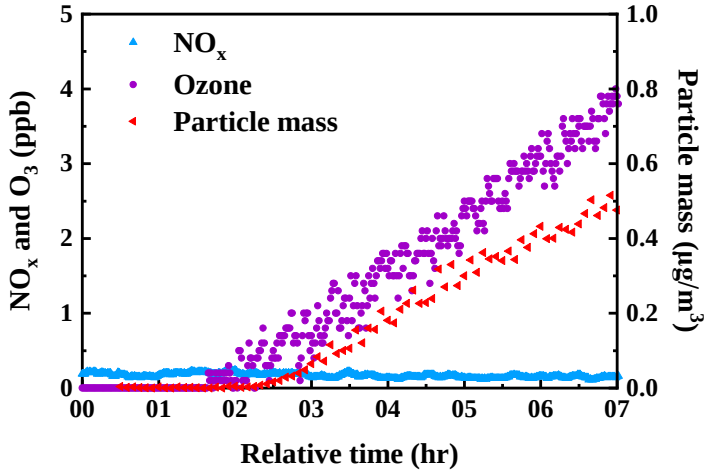


**Figure 3.** Concentrations of $NO_x$, Ozone and Particle number as a function of time during the photolysis of zero air.

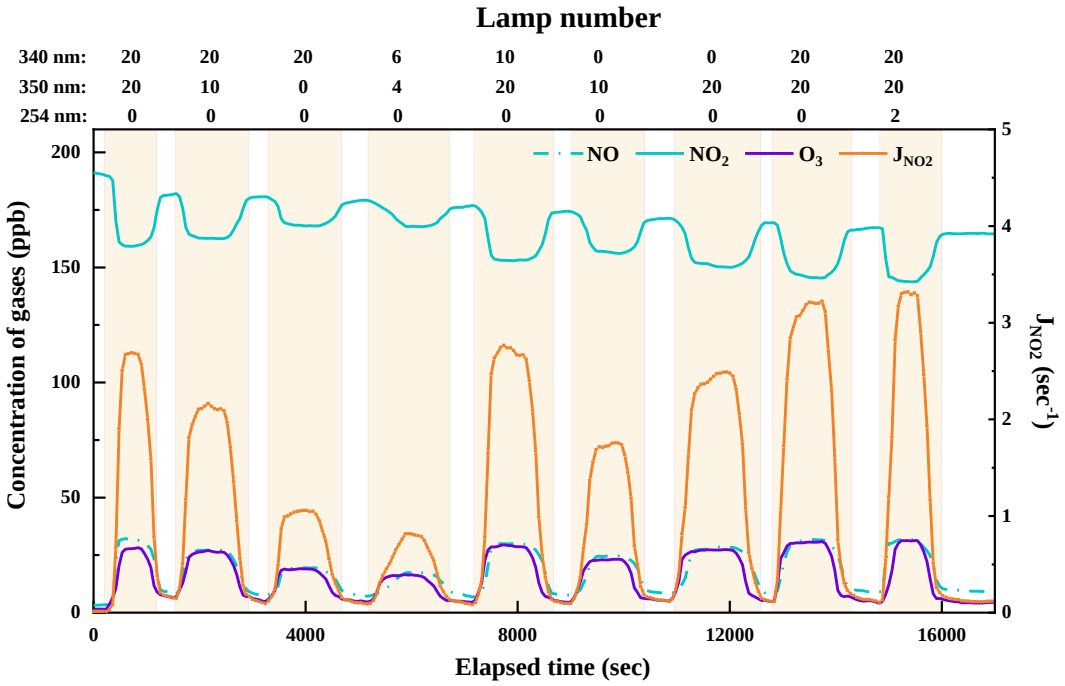


**Figure 4.** Variations of j($NO_2$) against concentrations of NO, $NO_2$ and $O_3$. The filled purple area means when a certain number of lights are turned on.

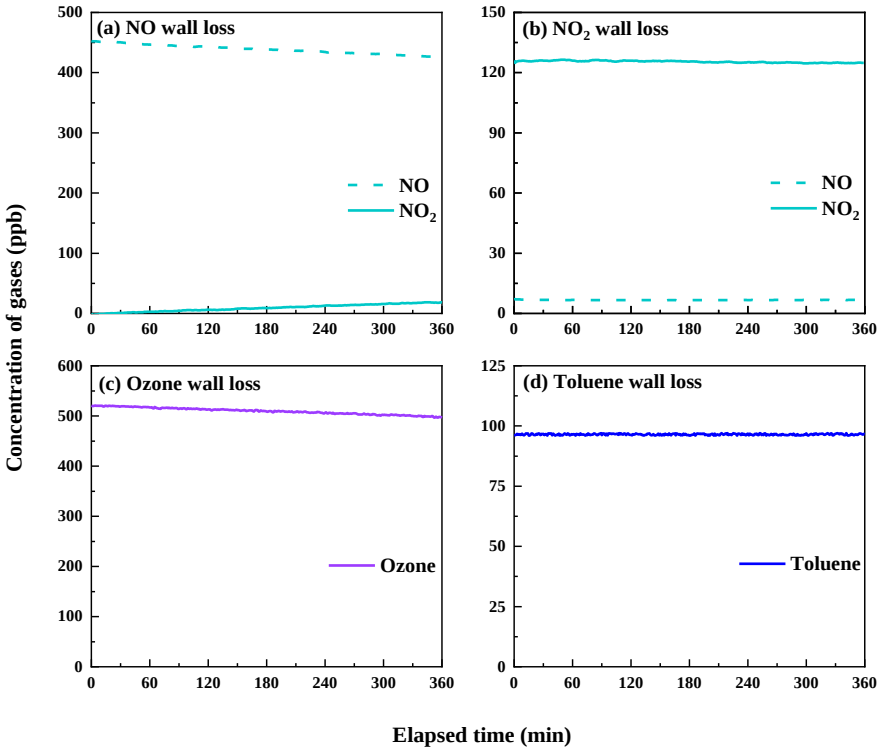


**Figure 5.** Experimental results for (a) NO, (b) $NO_2$, (c) $O_3$, (d) toluene wall loss.

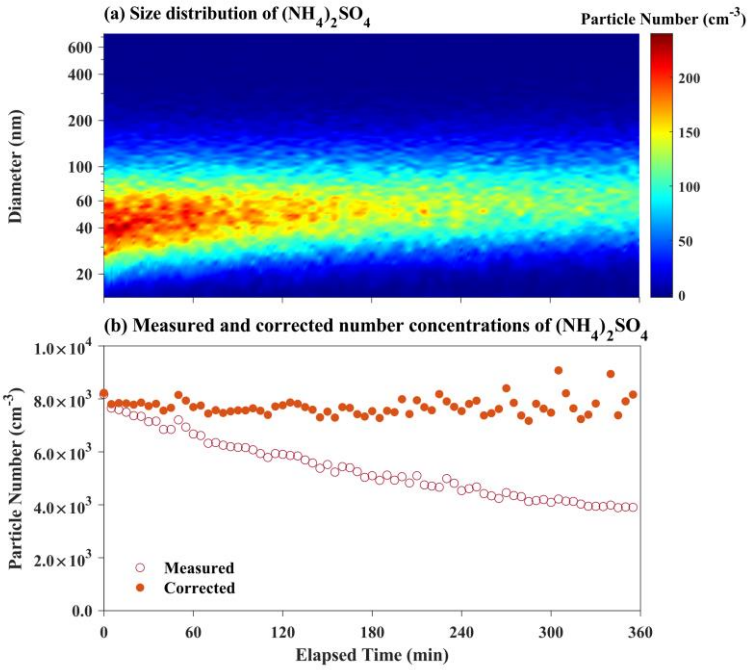


**Figure 6.** (a) Size distribution of $(NH_4)_2SO_4$ during a six-hours particle wall-loss experiment, (b) corrected particle number concentrations compared to measured particle number concentrations.

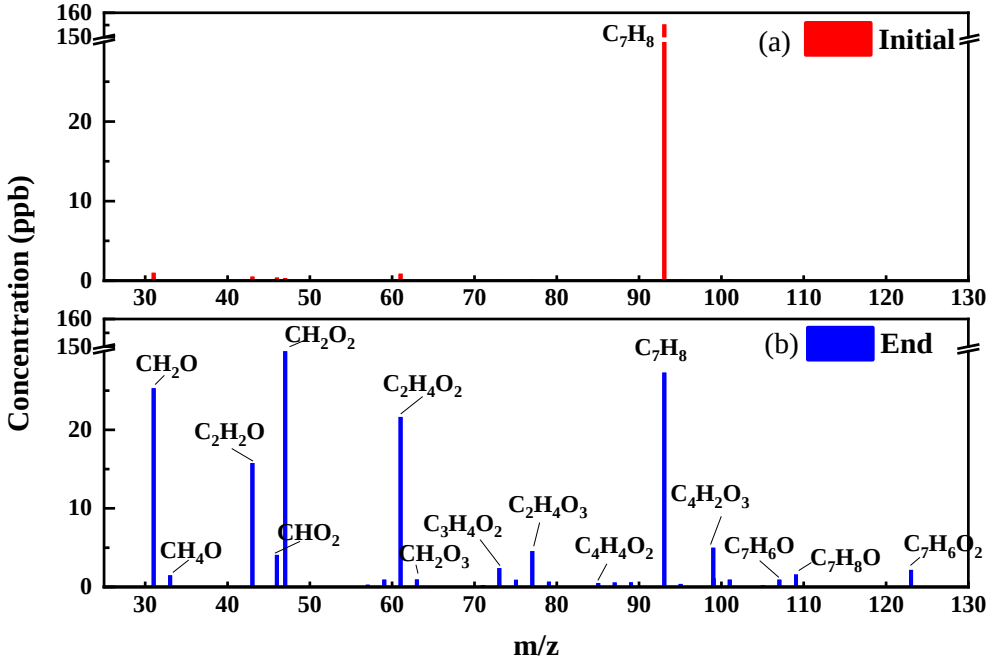


**Figure 7.** Mass spectra of VOCs detected by PTR-TOF-MS at the start (a) and the end (b) of toluene photooxidation experiment.

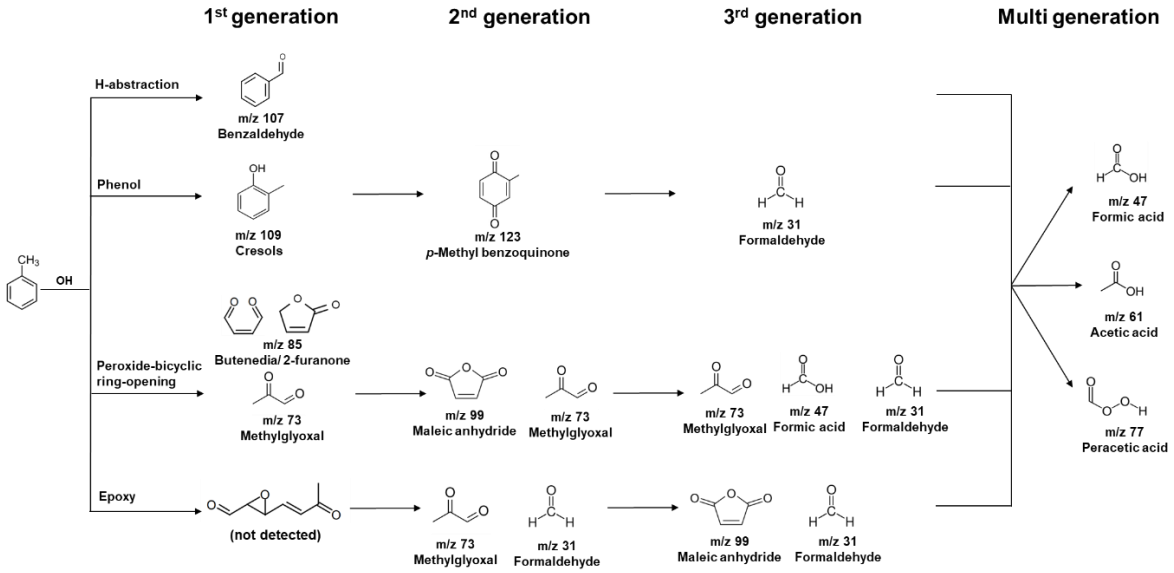


**Figure 8.** Major gas-phase products detected by PTR-TOF-MS in the toluene photooxidation system as implemented in the MCM v3.3.1.

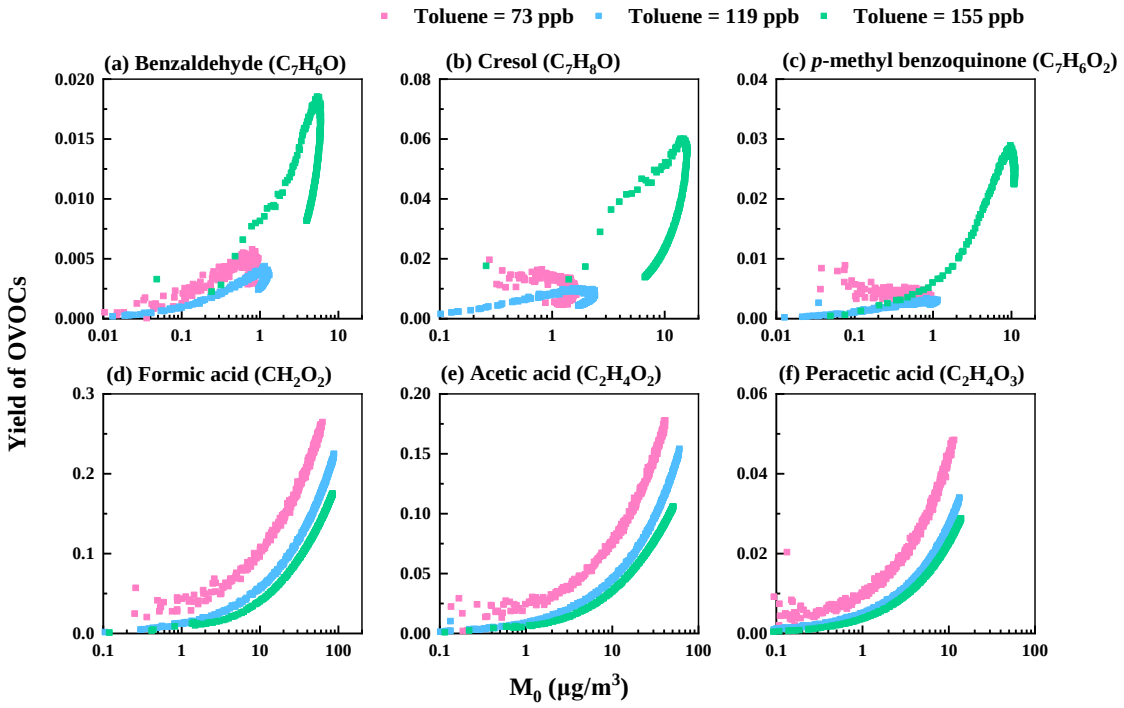


**Figure 9.** Yield of OVOCs in toluene-OH test.

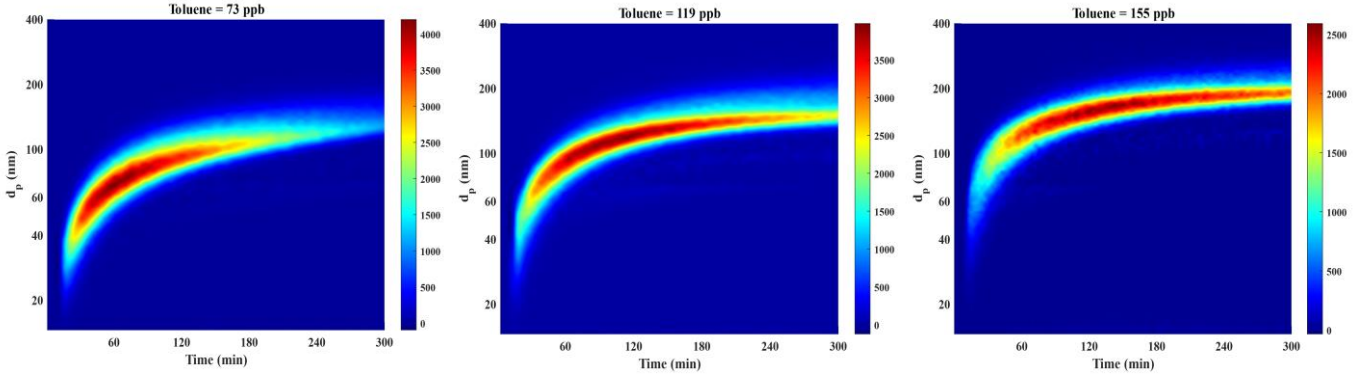


**Figure 10.** Variation of SOA size and number concentration for toluene photooxidation under different initial precursor concentration conditions.

**Table 1.** Overview of instruments.

| Instrument | Target species and parameters | Detection limit/ Range | Accuracy | Flow rate (L/min) |
|---|---|---|---|---|
| Teledyne Model T200U | $NO/NO_2/NO_x$ | < 50 ppt | 0.50% | 1 |
| Teledyne Model T400 | $O_3$ | 0.4 ppb | 0.5 ppb or 0.5% | 0.8 |
| Ionicon PTR-QiToF-MS | VOCs | < 10 ppt | ± 5% | 0.05–0.8 |
| Aerodyne HR-ToF-CIMS | Oxygenated VOCs | < 0.01 ppt | | 1.2–10 |
| Aerodyne Filter Inlet for Gases and AEROsols, FIGAERO | Particle composition | >10 ng | | 10 |
| SMPS (TSI 3082 DMA and 3776 CPC) | Particle number | $1–10^7$ $cm^{-3}$ | ± 3% | 0.3 |
| | Particle size | 10–1000 nm | ± 3% | |
| Custom built filter collector | Particle collection for offline analysis | | | 20 |
| Thermo Scientific LC- Orbitrap MS | Oxidation products in offline particulate samples | | <1 ppm | NA |
| Beijing Convenient Environmental Tech Co.Ltd sensors | Temperature | 10–40℃ | ± 1℃ | NA |
| | Relative humidity | 5%–85% | ± 3% | NA |
| | Pressure | 0-1000 Pa | ± 3 Pa | NA |

**Table 2.** Summary of wall loss rate of gas species and particle in PolyU chamber and comparison with other chamber facilities.

| **Chamber** | **Volume ($m^3$)** | **Surface to Volume Ratio ($m^{-1}$)** | **NO ($\times 10^{-4}$ $min^{-1}$)** | **$NO_2$ ($\times 10^{-4}$ $min^{-1}$)** | **$O_3$ ($\times 10^{-4}$ $min^{-1}$)** | **VOC ($\times 10^{-4}$ $min^{-1}$)** | **$k_{dep}$ at 100 nm ($\times 10^{-3}$ $min^{-1}$)** | **$J_{NO2}$ ($\times 10^{-3}$ $sec^{-1}$)** | **Reference** |
|---|---|---|---|---|---|---|---|---|---|
| PolyU | 5.4 | 1.59 | 0.47 | 0.37 | 1.17 | negligible (toluene) | 0.2 | 3.32 | This study |
| Tsinghua University | 2 | 5 | 3.38 | 4.17 | 6.07 | 0.06 | 2.6 | 3.83 | Wu et al. (2007) |
| KIST | 2.5 | | 7-20 | 4-20 | 12–24 | | | 2 | Bae et al. (2003) |
| Zhejiang University | 3 | 4.32 | | 1.64 | 8.99 | | 3.52 | 2 | Li et al. (2020) |
| CESAM, CNRS | 4.2 | 4.29 | | | 20 | < 0.6 (propene & isoprene) | 0.02–0.1 | 4.5 | Wang et al. (2011) |
| ICCAS-DRC | 5 | 3.59 | 3.0–3.1 | 3.8–4.5 | 2.5–3.1 | 0.31 (propene) | 2.0–4.3 | 2.32–2.55 | Wang et al. (2015) |
| Kyungpook National University | 7 | 3.09 | 3.78 | 4.48 | 6.47 | < 1.71 | 3.96 | 2.83 | Babar et al. (2017) |
| NCAT | 9 | 2.9 | 7.40 ± 0.01 | 3.47 ± 0.01 | 5.91 ± 0.08 | | 2.46 ± 0.11 | 2.75 ± 0.08 | Smith et al. (2019) |
| BUCT | 10 | 2.6 | 4.50−4.58 | 2.16−3.54 | 6.76−8.90 | 0.11-0.46 (toluene) | 1.33 | 6.67 ± 0.17 | Ma et al. (2022) |

**Table 3.** Summary of initial conditions and results for toluene photooxidation experiments.

| | **Toluene injection (ppb)** | **ΔHC (µg/m³)** | **$M_0$ of SOA (µg/m³)** | **Yield of SOA** | **$M_0$ of OVOCs (µg/m³)** | **Yield of OVOCs** |
|---|---|---|---|---|---|---|
| Test 01 | 73 | 198.79 | 29.0 | 24.7 | 103.49 | 0.52 |
| Test 02 | 119 | 336.11 | 71.0 | 26.4 | 197.92 | 0.59 |
| Test 03 | 155 | 465.14 | 165.3 | 34.3 | 287.12 | 0.62 |

**Table 4.** Summary of SOA yields in previous studies on toluene photooxidation at low or no $NO_x$ conditions.

| **$[Toluene]_0$ (ppb)** | **Δ[Toluene] (ppb)** | **PM (μg /m$^3$)** | **SOA yield** | **Reference** |
|---|---|---|---|---|
| 73 | 32 | 29.0 | 24.7% | **This study** |
| 119 | 72 | 71.0 | 26.4% | **This study** |
| 155 | 128 | 165.3 | 34.3% | **This study** |
| 1000 | – | 210 ± 20 | 15% ± 2% | Hinks et al. (2018) |
| 1000 | – | 87 ± 6 | 6.2% ± 0.5% | |
| 1000 | – | 84 | 5.9% | |
| 1000 | – | 28 ± 7 | 2.0% ± 0.5% | |
| 1000 | – | 26 ± 9 | 1.9% ± 0.6% | |
| 300 | – | 27 | 5.5% | |
| 300 | – | 9 | 2.2% | |
| 3980 | – | 127 | 7.58% | Sato et al. (2007) |
| 4004 | – | 97 | 5.61% | |
| 3998 | – | 92 | 5.87% | |
| 4074 | – | 109 | 4.55% | |
| 4005 | – | 104 | 6.31% | |
| 380 | – | 20 | 41% | Hildebrandt Ruiz et al. (2015) |
| 270 | – | 20 | 40% | |
| 180 | – | 20 | 66% | |
| 200 | – | 20 | 31% | |
| 570 | – | 20 | 26% | |
| 570 | – | 20 | 26% | |
| 690 | 306 | 93.9 | 8.15% | Chen et al. (2019) |
| 603 | 270 | 62.2 | 6.12% | |
| 425 | 245 | 42.6 | 4.61% | |
| 275 | 172 | 34.2 | 5.26% | |
| 66 | 39 | 12.6 | 8.44% | |
| 59 | 44 | 13.8 | 8.23% | |
| 37 | 25 | 7.2 | 7.76% | |
| 960 | 318 | 0 | 0% | Qi et al. (2020) |
| 990 | 511 | 87.1 | 4.3% | |
| 1010 | 553.7 | 168.9 | 8.4% | |
| 1010 | 596.2 | 291.5 | 12.1% | |
| – | 32.1 | 37.4 | 30.8% ± 1.7% | Ng et al. (2007) |
| – | 63.9 | 73.1 ± 5.6 | 30.2% ± 0.7% | |
| – | 10 | 11.5 ± 1.6 | 30.4% ± 4.1% | |
| – | 23.8 | 26.7 ± 2.5 | 29.8% ± 1.6% | |